



Enhanced superconductivity originating from f -electron doping in topologically nontrivial YPdBi half-Heusler thin films

Shivangi Srivastava,^{1,*} Bishal Das,^{2,*} Vishal Bhardwaj,³ Aftab Alam ,² Saroj P. Dash,⁴ and Ratnamala Chatterjee ^{1,5,†}

¹Department of Physics, Indian Institute of Technology Delhi, Hauz Khas, New Delhi-110016, India

²Department of Physics, Indian Institute of Technology Bombay, Mumbai 400076, India

³Department of Condensed Matter Physics, Weizmann Institute of Science, Rehovot 7610001, Israel

⁴Department of Microtechnology and Nanoscience, Chalmers University of Technology, SE 41296 Goteborg, Sweden

⁵National University of Science and Technology "MISIS," Leninsky Prospect 4, 119991 Moscow, Russia



(Received 3 January 2024; accepted 18 June 2024; published 15 July 2024)

YPdBi is a well-studied diamagnetic topologically trivial half-Heusler alloy that is superconducting with $T_c \sim 1$ K. When strained or in thin-film form, it shows a topologically nontrivial surface state with $T_c \sim 1.25$ K. ErPdBi is a well-studied topologically nontrivial half Heusler with $T_c \sim 1.22$ K. In this work, we demonstrate that the f -electron doping in YPdBi provides a unique way to selectively tune the electronic structure and aid in increasing the superconducting transition temperature of YPdBi. This work presents systematic measurements of electrical resistivity and magnetotransport on half-Heusler thin films of $Y_{(1-x)}Er_xPdBi$ ($x = 0.2, 0.5,$ and 0.8), prepared using the pulsed laser deposition technique. All the films were observed to be semimetallic, with a sharp downturn in resistivity at low temperatures $T < 5$ K; the E5 film ($T_c \sim 4.4$ K) and E8 film ($T_c \sim 3.7$ K) reach a zero-resistivity value, within the experimental limit. The doping of f electron on Y^{+3} sites possibly gives rise to the improved Fermi parameters and an increase in T_c . Magnetoresistance measurements and first-principle calculations support that $Y_{(1-x)}Er_xPdBi$ are topologically nontrivial semimetals. The first-principle calculations also show that with an increase in the doping concentration (x), more f bands start to appear near Fermi level (E_F), giving rise to an increase in the band-inversion strength due to s - f exchange interaction. The nontrivial band structure, odd-parity Cooper pair, and noncentrosymmetric crystal structure suggest the presence of unconventional superconductivity in the E5 and E8 films.

DOI: [10.1103/PhysRevMaterials.8.075001](https://doi.org/10.1103/PhysRevMaterials.8.075001)

I. INTRODUCTION

The f -electron doping in ternary half-Heusler (HH) YPdBi, with noncentrosymmetric MgAgAs cubic structure ($F\bar{4}3m$, space group 216), provides a unique way to selectively tune the electronic structure in a way that may prove to be useful for designing future spintronics and quantum computing devices. A tuning of the s - and p -like band inversions via the atomic number (tailored by changing the constituent element) or spin-orbit coupling strength may not only lead to topologically nontrivial phases in some of them but also can provide a pathway to systematically study the coexistence of competing superconducting and magnetic orders [1–5]. In addition, the stabilization of magnetic and superconducting ground states in $RPdBi$ (R is rare-earth element), along with the topological nontriviality, makes these semimetals promising candidates to host collective excitations involving relativistic carriers like Dirac-Weyl-Majorana fermions with high mobility, very high magnetoresistance (MR), and dissipationless transport [6]. Transport studies of HH alloys are also relevant due to their high charge-to-spin conversion efficiency or spin Hall angle for practical spintronic applications [7].

In recent years YPdBi [8,9] and some other alloys like LuPdBi [10,11], TbPdBi [8,12], and ErPdBi [13,14] have been shown to exhibit superconductivity at low temperatures ($T_c \leq 2$ K), owing to their noncentrosymmetric structure. These HH alloys exhibit a unique quasilinear temperature fluctuation of the upper critical field and penetration depth, rendering unconventional superconducting properties [2,10,11,13].

The HH YPdBi (YPB) is an established topologically trivial diamagnetic alloy that can be driven to a nontrivial state by applying strain [1,9,15]. On the other hand, ErPdBi (EPB) [13,14] is a topologically nontrivial semimetal that has been reported to exhibit the coexistence of magnetic ordering ($T_N \sim 1.06$ K) and superconductivity ($T_c \sim 1.22$ K). In the present paper, the diamagnetic YPdBi system is partially substituted with Er^{+3} ions at Y sites. The Clementi-Raimondi z_{eff} of Er ($4f$) is 27.98, which is considerably larger than Y ($4d$), 15.96, and thus the effect of Er substitution in YPB is to enhance the band-inversion energies ($\Delta E = \Gamma_8 - \Gamma_6$) in the system [8]. The resistivity and magnetotransport behavior of $Y_{(1-x)}Er_xPdBi$ (YEPB) [110]-oriented strained nontrivial thin films on [100] MgO substrates with $x = 0.2, 0.5,$ and 0.8 are reported in this work. From now onwards, the compositions $Y_{0.8}Er_{0.2}PdBi$, $Y_{0.5}Er_{0.5}PdBi$, and $Y_{0.2}Er_{0.8}PdBi$ will be referred as E2, E5, and E8, respectively. In our earlier work, we observed a sharp drop in the resistivity around

*These authors contributed equally to this work.

†Contact author: ratnamalac@gmail.com

2.2 K in strain-driven nontrivial thin films of YPB [9], and a similar downturn was noted around 3 K in the resistivity of nontrivial thin films of EPB [14]. In the present work, we report an enhanced superconducting transition (T_c) ~ 4.4 K in equidoped E5 film. The magnetotransport behavior of all YEPB films reveals nontrivial 2D band structures with Berry phase $\sim \pi$. Density-functional theory (DFT) calculations in bulk YEPB samples show clear band inversion between Γ_8 and Γ_6 bands, further confirming nontrivial band topology in all three compositions.

II. EXPERIMENTAL DETAILS

A custom-designed water-cooled rf induction melting furnace was used to prepare the bulk samples of YEPB alloys in a continuous Ar gas flow maintained using a vacuum pump. High-purity Y ingots (99.99%), Er ingots (99.95%), Pd ingots (99.99%), and Bi chunks (99.99%) were melted together in a rf induction melting furnace in a molar ratio of $(1-x):x$ ($x = 0.2, 0.5, \text{ and } 0.8$):1:3, respectively. Using a Panalytical X'pert Highscore x-ray diffractometer configured with a Cu K_α (1.541 Å) radiation source, the x-ray diffraction (XRD) patterns of polycrystalline bulk samples of YEPB were obtained at room temperature. Thin films of samples were grown on a single crystal of [100]-oriented MgO with a seed layer of ~ 5 nm β -Ta [16], using the pulsed laser deposition (PLD) under a base pressure of 5×10^{-7} Torr; the chamber was repeatedly flushed with Ar gas before the final deposition at base pressure. Parameters like laser fluence, and substrate-to-target distance were optimized to get the desired thickness and phase of the film at the substrate temperature of 260 °C. The surface morphology of the thin films was recorded on a Bruker Dimension 3100 atomic force microscope. For determining the stoichiometry of films, we used the TESCAN Magna LMU field-emission scanning electron microscope equipped with an energy-dispersive x-ray spectrometer (EDS). The magnetic measurements of thin films were made using Cryogenic Limited's cryogen-free magnetometer system in the temperature range of 2 to 300 K equipped with a ± 14 T magnet. The (3×10) mm² films in the standard four-probe geometry were used for magnetotransport measurements. A Keithley 2400 source meter was used to supply a 50 μ A dc current, and the Keithley nanovoltmeter was utilized to measure the potential difference.

III. COMPUTATIONAL DETAILS

We have performed first-principles DFT [17,18] calculations for bulk $Y_{(1-x)}Er_xPdBi$ ($x = 0, 0.25, 0.50, 0.75, \text{ and } 1$) using the Vienna *Ab initio* Simulation Package (VASP) [19–21] based on the projector-augmented wave [22,23] method. A plane-wave energy cutoff of 350 eV was used, and relativistic spin-orbit coupling was included in all the calculations. The exchange-correlation energy was described within the generalized gradient approximation following the Perdew-Burke-Ernzerhof [24] prescription. The simulated alloying concentrations, $x = 0.25, 0.50, \text{ and } 0.75$, are close to the experimental concentrations of E2, E5, and E8 samples, respectively.

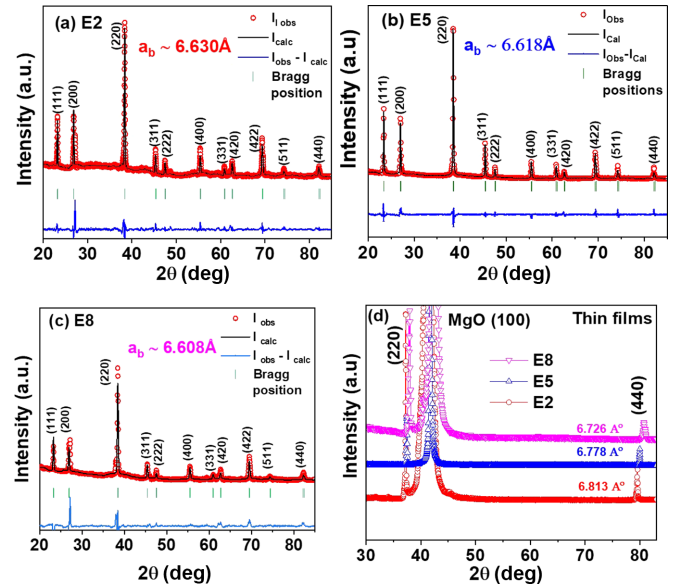


FIG. 1. (a)–(c) The room-temperature powder x-ray diffraction pattern (red circles) of polycrystalline samples, with the Rietveld refinement profiles, and the fitted Bragg peak positions. (d) X-ray diffraction pattern of thin films.

Bulk electronic structure calculations have been carried out in a $2 \times 2 \times 2$ supercell of the primitive unit cell (henceforth referred to as the simulation unit cell) of face-centered cubic (fcc) lattice using the experimental lattice parameters. The Brillouin zone (BZ) integration was done on a Γ -centered $4 \times 4 \times 4$ k -mesh using the tetrahedron method with Blöchl corrections and the total energy convergence criterion was set to 10^{-6} eV. The band structures have been calculated within the primitive BZ at the following high-symmetry k points: $L = (1,1,1)$; $\Gamma = (0,0,0)$, and $X = (1,0,1)$. The semi-core s orbitals of Y have been treated as valence due to the possibility of band hybridization. The f orbitals of Er have been treated as valence since they are crucial to capture the intricate physics involving magnetism. A Hubbard- U correction of $U_{\text{eff}} = U - J = 6.0$ eV was applied to the f electrons using Dudarev's approach [25] implemented within VASP, in accordance with available literature [26–28].

To simulate the surface dispersion, bulk electronic structure calculations (keeping all *ab initio* parameters the same) were done using the strained thin-film lattice parameters and a tight-binding bulk Hamiltonian was obtained within the maximally localized Wannier functions (MLWF) scheme [29–31] using the WANNIER90 [32–34] package. The atomic orbital projections of Bi (s, p), Pd (s, p, d), Y (d), and Er (d, f) were used to construct the MLWFs. Finally, using the tight-binding bulk Hamiltonian, iterative Green's function method [35–37] was applied to calculate the surface dispersion for a slab containing 40 atomic layers as implemented in the WANNIERTOOLS [38] package.

IV. RESULTS AND DISCUSSIONS

Figures 1(a)–1(c) show the Rietveld-refined room-temperature powder XRD patterns of YEPB polycrystalline bulk samples. The Rietveld refinements using the FULLPROF

software confirm the ($C1_b$) cubic crystal structure (space group $F\bar{4}3m$, 216) without any secondary phase, within the instrument's sensitivity limit. We observed a decrease in the lattice constant of the polycrystalline unit cell from 6.630 Å $\leq a_b \leq$ 6.608 Å, with an increase in Er concentration. This is expected as the ionic radius of Er^{+3} (1.004 Å, coordination No. 8) is smaller than the ionic radius of Y^{+3} (1.019 Å, coordination No. 8) [39]. Figure 1(d) shows the room-temperature x-ray diffraction of thin films in Bragg-Brentano geometry, where only the symmetric (220) and (440) Bragg's reflections are observed, suggesting that the films are preferentially oriented along the [110] direction. In view of the fact that the emphasis of the work is to demonstrate the superconducting nature of the films, absence of any peak at or around $2\theta \sim 33.26^\circ$ (with Cu K_α radiation source), either in bulk polycrystalline [Figs. 1(a)–1(c)] or in thin film [Fig. 1(d)], confirms the absence of superconducting binary PdBi phase [$H_{c2}(0) \sim 0.8\text{T}$] [40]. From XRD data, the lattice constants of thin films (a_{TF}) were calculated to be 6.813, 6.778, and 6.726 Å, for E2, E5, and E8, respectively. A shift in the peak position towards a higher 2θ side with increasing Er content was observed accordingly. Thickness of the films (~ 29 nm) and surface roughness, ~ 1 to 2 nm, estimated from X-ray reflectivity measurements and atomic force microscopy images, are shown in Fig. S1 and Table S1 in the Supplemental Material [41]. The thin-film compositions reported here were determined using the EDS technique. Figures S2(a)–S2(c) of the Supplemental Material [41] show the EDS spectra for films E2, E5, and E8, respectively.

Figure 2(a) shows the temperature-dependent electrical resistivity $\rho_{xx}(T)$ in longitudinal geometry of YEPB films in the temperature range $2\text{ K} \leq T \leq 10\text{ K}$. We observe that in the measured temperature range, the resistivity decreases with an increase in Er concentration. This observation can possibly be attributed to an increase in the number of conduction-band electrons in YEPB films, contributed by the addition of Er [8,42]. It is interesting to note that all YEPB films show a sharp downturn in $\rho_{xx}(T)$, which reaches a zero-resistivity value for the films E5 and E8. In the literature [9,10,14], the criterion of designating the superconducting transition temperature T_c (in K) in HH alloy systems is usually taken as the point where the $\rho_{xx}(T)$ falls to 90% of the normal steady-state resistivity value. The T_c 's of E2, E5, and E8 films, thus estimated from Fig. 2, are $T_{E2} \sim 2.2\text{ K}$ (extrapolated), $T_{E5} \sim 4.4\text{ K}$, and $T_{E8} \sim 3.7\text{ K}$, respectively. For E2 film, the $\rho_{xx}(T)$ is extrapolated down to zero ρ_{xx} using the Levenberg-Marquardt iteration algorithm (nonlinear asymptotic model $\rho_{xx} = a - bc^T$), where a , b , and c are fitting parameters, and T is temperature). The robust nature of superconductivity is reflected in the ac susceptibility magnetic measurements of the polycrystalline samples, which show a similar trend of T_c 's as in films; see Fig. S3 in the Supplemental Material [41].

In order to confirm the superconducting nature of the thin films, we performed the dc magnetic measurements on the representative E5 film of dimension $2\text{ mm} \times 3\text{ mm} \times 29\text{ nm}$ having highest $T_c \sim 4.4\text{ K}$, with magnetic field perpendicular to the plane of film. A clear diamagnetic signal observed in zero-field-cooled (ZFC) curve suggests a bulk

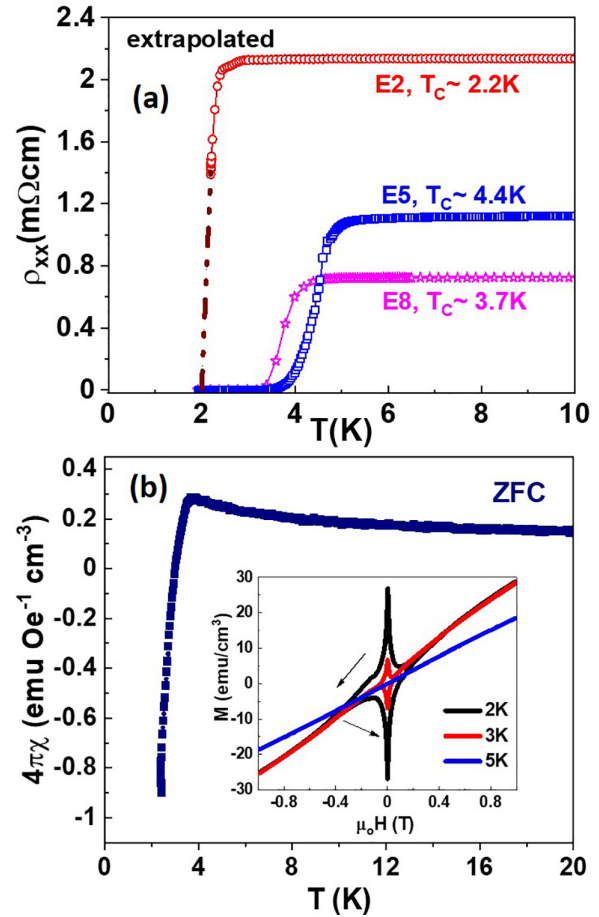


FIG. 2. (a) The ρ_{xx} vs T plot for thin films in the temperature range of $2\text{ K} \leq T \leq 10\text{ K}$ at zero magnetic field for E2, E5, and E8 films, (b) Low-temperature dependence of dc magnetic susceptibility under magnetic field of 50 Oe in ZFC for E5 thin film. Inset: Magnetization vs magnetic field at low temperature under ZFC.

superconductivity of this film; see Fig. 2(b). The inset of Fig. 2(b) shows the magnetization vs magnetic field at low temperatures under ZFC. Clear hysteresis peaks around zero field can be seen at low temperatures 2 K, and 3 K ($T < T_c$), whereas the 5 K ($T > T_c$) data of the film shows the paramagnetic/compensated antiferromagnetic nature. In order to validate that the superconducting transition temperature of the E5 film ($T_c \sim 4.4\text{ K}$) is originating from the E5(29 nm)/Ta(5 nm)/MgO, the magnetization vs temperature measurements on Ta(5 nm)/MgO substrate were also performed (see Fig. S4(a) of the Supplemental Material [41]), and this substrate clearly shows an absence of diamagnetic signal. In thin superconducting films, demagnetization effects may cause an overshoot of the external magnetic field at the sample's edges, which may break down the Meissner state even in very small applied fields and may allow vortices to penetrate [43]. To account for the demagnetization factor (N), we performed low-field magnetization measurements as a function of field at 2 K (see Fig. S4(b) [41]) for the E5 film [44] and observed $N \sim 1$. The calculated N is consistent with the sample shape (thin film) and the configuration (applied field perpendicular to the plane of the film) of the measurement.

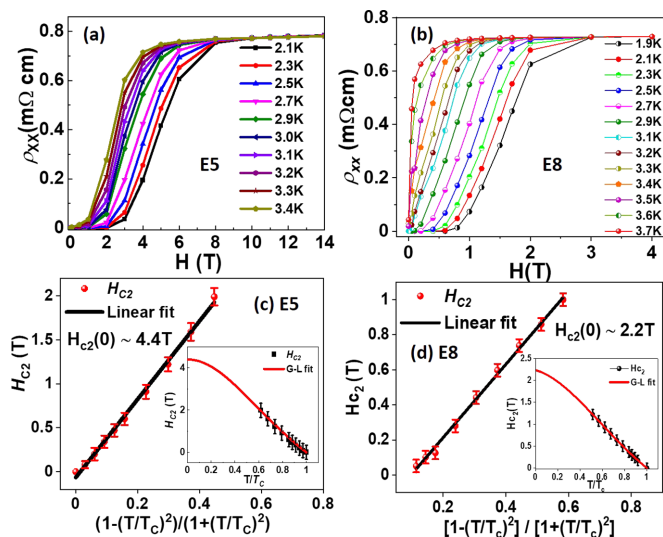


FIG. 3. The field-dependent longitudinal resistivity $\rho_{xx}(T)$ vs magnetic field: (a) E5 sample, (b) E8 sample; (c) and (d) show $H_{c2}(0)$ for E5 and E8 films, solid black line represents the linear fit: Inset: shows the G-L fit of E5 and E8 films.

We extracted the upper critical field from the resistivity vs magnetic field data at different temperatures with the magnetic field applied perpendicular to the plane of the films, as shown in Figs. 3(a) and 3(b), for E5 and E8 films, respectively. The values of the upper critical field at absolute zero temperature, $H_{c2}(0)$, estimated via the slope approach using the Ginzburg-Landau model, are 4.4 and 2.2 T for E5 and E8 films, respectively. The linear fitting yields the $H_{c2}(0)$ as the slope, shown in Figs. 3(c) and 3(d).

$$H_{c2}(T) = H_{c2}(0) \times \left[1 - \left(\frac{T}{T_c} \right)^2 \right] / \left[1 + \left(\frac{T}{T_c} \right)^2 \right].$$

We also determined the zero-temperature limit of the upper critical field $H_{c2}(0)$ with the second approach by fitting $H_{c2}(T)$ vs T/T_c data to the generalized Ginzburg-Landau model [the red solid lines in the inset of Figs. 3(c) and 3(d)], with the $H_{c2}(0)$ as the fitting parameter [5,45,46]. Both the approaches yield approximately the same value of $H_{c2}(0)$. The fitted values of $H_{c2}(0)$ for our films are comparable to those obtained for other topological superconductors and noncentrosymmetric systems (2.9 T for LuPdBi [11] and 2.4 T for TbPdBi [12] [9,10,14]. Unusual linear temperature dependence of $H_{c2}(T)$ plot, shown in the inset of Figs. 3(c) and 3(d) for E5, and E8 films, follows a trend similar to the topological superconductors and noncentrosymmetric systems reported in literature [10,12,13,45]. Using the value of $H_{c2}(0)$, we evaluated the superconducting coherence length ξ_0 at 8.6 nm (E5 film) and 12 nm (E8 film) using the zero-temperature relation $\xi_0 = \sqrt{\frac{\Phi_0}{2\pi H_{c2}}}$, where $\Phi_0 = 2.07 \times 10^{-15} \text{ T m}^2$ is the flux quantum. The mean-free path of carriers $l \sim 98$ nm (E5 film), and $l \sim 71$ nm (E8 film) are estimated from Shubnikov-de Haas (SdH) oscillations and $\frac{\xi_0}{l} \ll 1$, which indicate our samples is in the clean limit [47]. Using the Werthamer-Helfand-Hohenberg formula $H_{\text{orb}} = -0.72 \frac{dH_{c2}}{dT} \times T_c$, we approximated the zero-temperature critical orbital field for the films, 3.7 T (E5 film) and 1.6 T (E8 film), respectively. The Pauli-limiting field (H_P)

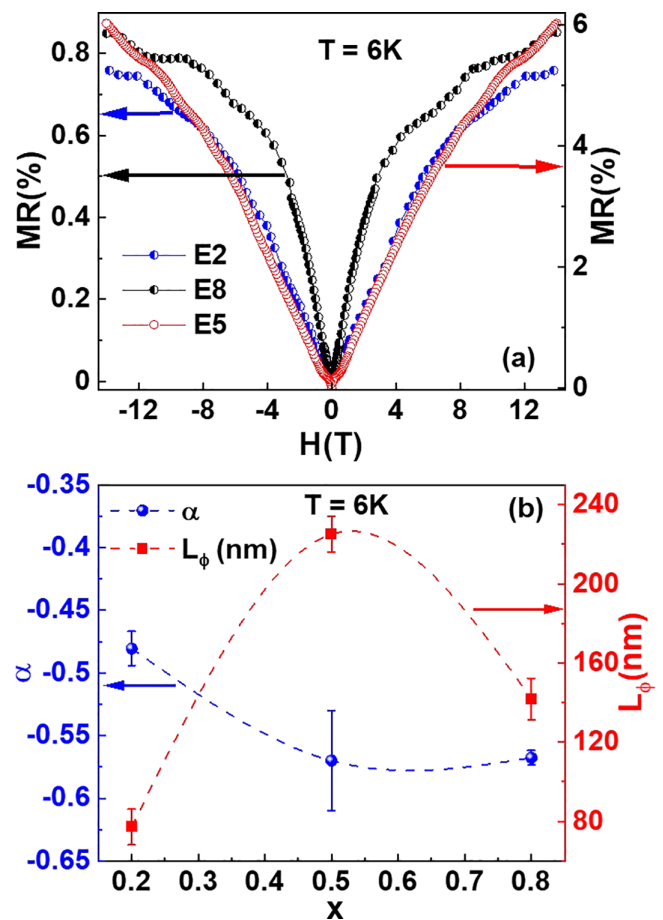


FIG. 4. (a) MR data of E2, E5, and E8 at 6 K. (b) The HLN fitted parameters (α , L_ϕ) as a function of Er doping concentration (x) of E2 ($x = 0.2$), E5 ($x = 0.5$), and E8 ($x = 0.8$) films at 6 K.

is evaluated using the relation $H_P = 1.76 \times \frac{k_B}{\sqrt{2}\mu_B} \times T_c$, as H_P is 6.3 T (E5) and 6.8 T (E8). Since $H_{\text{orb}} < H_{c2}(0) < H_P$, superconductivity in E5 and E8 films is Pauli limited, and similar relationship was established for unconventional HH superconductors LuPdBi [10], TbPdBi [12], YPtBi [44], and LuPtBi [45].

The low-temperature longitudinal MR = $[\rho(H) - \rho(0)]/\rho(0)$ [48,49] was measured in four-probe geometry in the magnetic field range $-14 \text{ T} \leq H \leq 14 \text{ T}$, and in the temperature range $T > T_c$ (see Fig. S5 in the Supplemental Material [41]). The magnetic field was applied perpendicular to the plane of the YEPB films. The MR data of films E2, E5, and E8 at 6 K (above the T_c^{onset} of all films) in the range $(-14 \text{ T} \leq H \leq 14 \text{ T})$ are shown in Fig. 4(a). The MR% (at 6 K) is maximum, $\sim 6\%$ (at $H = \pm 14 \text{ T}$) for optimally doped E5 film. The distinctive features in present MR data in the YEPB films are (i) a sharp rise in magnetoresistance near the origin (low field), indicating weak antilocalization (WAL) effect; (ii) SdH oscillations in resistivity at high magnetic fields, which are widely reported in topological insulators and topological semimetals [49,50]. Furthermore, the magnetoconductance data are investigated to identify the parameters that define the WAL effect and control the conductivity mechanism in the YEPB films

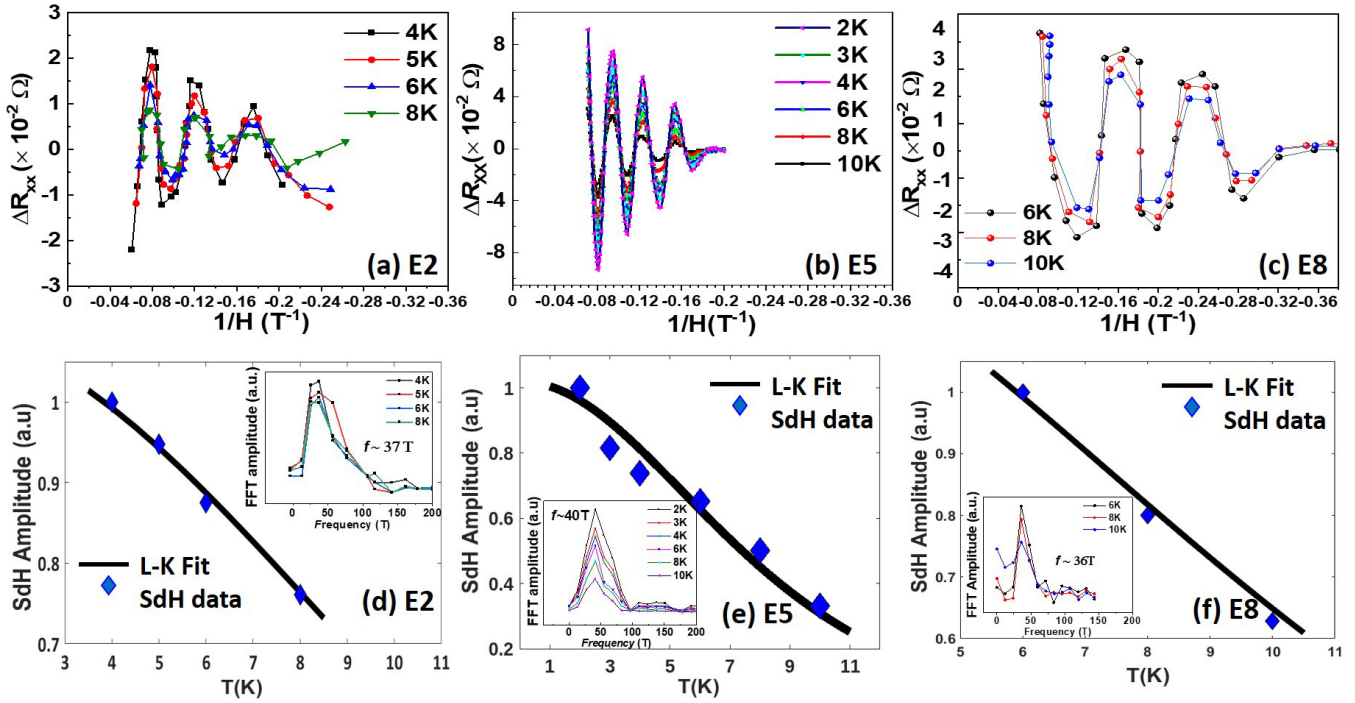


FIG. 5. SdH oscillations as a function of $1/H$, after subtracting the background contribution for (a) E2, (b) E5, and (c) E8 films; (d)–(f) A fitting of SdH oscillation amplitude to LK formula at constant magnetic field. Insets depict the FFT amplitudes vs frequency plots of E2, E5, and E8 films.

using the well-known Hikami-Larkin-Nagaoka (HLN) model [51]; see Figs. S6(a)–S6(c) [41]. The extracted fitting parameters prefactor (α) and coherence length (L_φ) for all three films at $T = 6$ K (above the T_c^{onset} of all films) are shown in Fig. 4(b). We noticed that the values of α are -0.48 , -0.57 , and -0.56 for E2, E5, and E8 films, respectively, are close to -0.5 , attributing single-surface conduction in YEPB films. The L_φ measured at 6 K are 77, 225, and 141 nm, for E2, E5, and E8 films, respectively. We observed that $L_\varphi \sim 225$ nm is maximum for optimally doped E5 film, reflecting a minimum dephasing of carriers compared to other doped films. The temperature dependence of coherence length L_φ follows a power-law fitting: $L_\varphi \propto T^{-p}$, with $p = 1/2$ for 2D systems [52]. The power-law fit of L_φ with temperature of the YEPB films yields p around 0.5, shown in Fig. S7 [41], indicating the 2D topological nature of YEPB films.

In the field-dependent resistivity of E2, E5, and E8 samples, we have observed SdH oscillations at low temperatures (≤ 10 K) for magnetic fields in the range ~ 4 –14 T (see Figs. S5(a)–S5(c) [41]) and plotted ΔR_{xx} (ΔR_{xx} has been determined by subtracting the polynomial background from R_{xx}) as a function of an inverse magnetic field at different temperatures, shown in Figs. 5(a)–5(c). The temperature dependence of SdH oscillations is fitted to the following Lifshitz-Kosevich (LK) expression [50,53,54]:

$$\sigma_{xx} \propto \frac{\lambda}{\sinh(\lambda)} e^{-\lambda_D} \cos 2\pi \left(\frac{f}{B} + \beta - \delta \right),$$

with $\lambda = \frac{2\pi^2 k_B T m^*}{\hbar e B}$ and $\lambda_D = \frac{2\pi^2 k_B T_D m^*}{\hbar e B}$. Here, f is the frequency of SdH oscillation obtained after carrying out the fast

Fourier transform (FFT) of the plot ΔR_{xx} vs $1/H$, $2\pi\beta$ is the Berry phase, T_D is the Dingle temperature, m^* is the effective mass of the electron, and δ is a dimensionless parameter, which takes the value ~ 0 for 2D systems, and $\pm 1/8$ for 3D systems [53]. In our case, the YEPB films possess 2D topological surface states, which allow us to consider $\delta \sim 0$. The temperature-dependent SdH oscillation amplitude at a fixed magnetic field with $\sigma_{xx} \propto \frac{\lambda}{\sinh(\lambda)}$, shown in Figs. 5(d)–5(f), yields the effective mass (m^*) of the Dirac electrons, and magnetic field-dependent term at a constant temperature $\sigma_{xx} \propto e^{-\lambda_D}$ gives Dingle temperature [50,52], shown in Fig. S8 of the Supplemental Material [41]. The calculated effective mass is 0.13, 0.20, and 0.13 m_e (m_e : mass of free electron) for the E2, E5, and E8 samples, respectively, which are consistent with those previously reported for RPdBi [9,11,14,48,52]. The FFT amplitudes of the SdH oscillations are plotted as a function of frequency and the prominent peak of the oscillation exists at 37, 40, and 36 T for E2, E5, and E8 samples, respectively; see insets of Figs. 5(d)–5(f). Using the Onsager relation [55], $f = \frac{\hbar}{2\pi e} A_F$, the extremal cross section of the Fermi surface (A_F) is calculated (see Table I). Considering the Fermi-surface cross section to be circular, $A_F = \pi k_F^2$, we calculated the Fermi wave vector k_F . The Fermi velocity $v_F = \hbar k_F / m^*$, and the position of Fermi level from the linear dispersion nodes, were also calculated using m^* and k_F values [$E_f^s = (\hbar k_F)^2 / m^*$] (see Table I). The sheet-carrier density ($n_{2D} = k_F^2 / 4\pi$) is also extracted from SdH oscillations. The transport lifetime (τ), mean-free path (l), quantum mobility of carriers (μ_s), and Landau level (LL) broadening (Γ), are calculated using the relations $\tau = \hbar / (2\pi T_D)$, $l = v_F \tau$, ($\mu_s = e\tau / m^*$), and $\Gamma = \pi k_B T_D$; see Table I [50,52].

TABLE I. Summary of electronic parameters of YEPB thin films obtained from fitting of the SdH oscillations data to Lifshitz-Kosevich theory. Here, f : frequency of SdH oscillations; n_{2D} : sheet-carrier density; m^* : effective mass of carriers; k_F : Fermi wave vector; v_F : Fermi velocity; E_f^s : position of linear dispersion node from Fermi level; T_D : Dingle temperature; Γ : LL broadening; τ : transport lifetime, l : mean-free path; μ_s : quantum mobility of carriers; and $2\pi\beta$: Berry phase.

Parameters	E2	E5	E8
$f(T)$	37	40	36
n_{2D} (10^{11}cm^{-2})	8.97	9.75	8.67
m^* (m_e)	0.13	0.20	0.13
k_F (\AA^{-1})	0.034	0.035	0.033
v_F (10^5ms^{-1})	2.99	2.02	2.86
E_f^s (meV)	67	47	62
T_D (K)	4.6	3	5.5
Γ (meV)	1.24	0.82	1.48
τ (10^{-13} s)	2.64	4.05	2.21
l (nm)	79	98	71
μ_s ($\text{cm}^2\text{V}^{-1}\text{s}^{-1}$)	3533	4429	2910
$2\pi\beta$, (π) \pm 0.1	0.98	0.92	0.86

The calculation of various SdH parameters for all the samples hints low LL broadening, large τ , and high quantum mobility ($4429\text{cm}^2\text{V}^{-1}\text{s}^{-1}$) of the E5 film, compared to other HH topological semimetals like HoPdBi ($501\text{cm}^2\text{V}^{-1}\text{s}^{-1}$) [56], DyPdBi ($1780\text{cm}^2\text{V}^{-1}\text{s}^{-1}$) [52], ErPdBi ($1035\text{cm}^2\text{V}^{-1}\text{s}^{-1}$) [14], and YPdBi ($3694\text{cm}^2\text{V}^{-1}\text{s}^{-1}$) [9], hints at the minimum scattering of Dirac

Fermions in E5 film. The analysis of the cosine part of the LK formula provides evidence of the nonzero Berry phase ($2\pi\beta$) for all films. We extracted the Berry phase from the LL fan diagram, which is LL index n vs $1/H$ as shown in Fig. S9 [41]. Here, while indexing we followed the minima in resistivity corresponding to integer values n , and the maxima correspond to $n + 1/2$. The intercept of the linear fit of LL index (n) vs $1/H$, at the n axis, gives $\beta \sim 0.5$, i.e., Berry phase ($2\pi\beta$) $\sim \pi$ for all three samples. The extracted π Berry phase for all three films from the LL fan diagram suggests the presence of Dirac fermions originating due to the nontrivial nature of the YEPB films. Additionally, possible compensated magnetic order in YEPB films can make them promising candidates for spintronic applications. Materials with antiferromagnetic (AFM) order are known to show exchange-bias effect when interfaced with ferromagnetic (FM) materials (typically used as active materials in spintronic devices) and can be used as pinning layers to “fix” the magnetic ordering of an interfaced FM layer. This effect has primarily been used in demonstrating enhancement of practical spintronic devices such as spin valves, magnetic tunnel junctions, etc. [57–59]. AFM materials are also being used for terahertz spintronics applications due to their high characteristic resonance frequencies enabling fast switching between spin states [60–62].

To understand the topologically nontrivial nature of $\text{Y}_{(1-x)}\text{Er}_x\text{PdBi}$, we have performed first-principles calculations of the pure- and mixed-alloy systems. Figure 6(a) shows the crystal structure of $\text{Y}_{(1-x)}\text{Er}_x\text{PdBi}$ and the simulation unit cell (also see Fig. S10 of the Supplemental Material [41]). Figures 6(b)–6(f) show the bulk band structures of

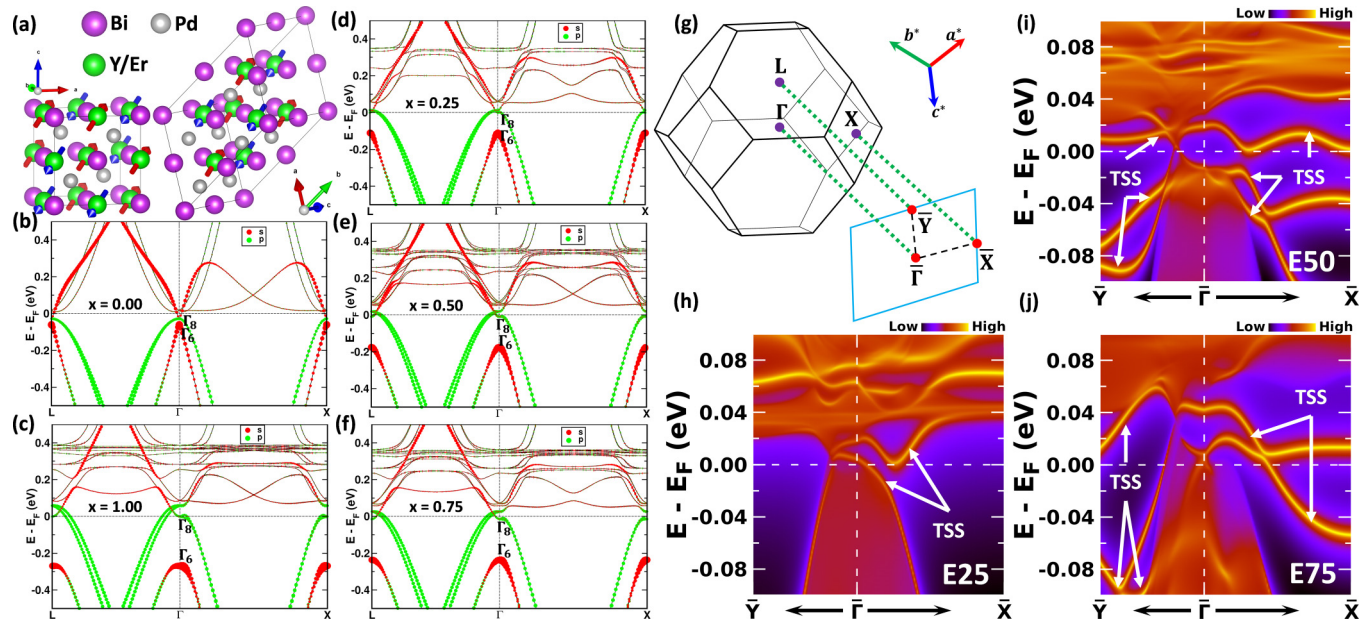


FIG. 6. Crystal structure of $\text{Y}_{(1-x)}\text{Er}_x\text{PdBi}$ shown in (a) cubic conventional cell (left) and $2 \times 2 \times 2$ supercell of the primitive unit cell of fcc lattice (right) along with AFM2 ordering. The arrows denote the direction of magnetic moments on Er atoms. Bulk band structure of $\text{Y}_{(1-x)}\text{Er}_x\text{PdBi}$ at experimental bulk lattice parameters for (b) $x = 0$, (c) $x = 1$, (d) $x = 0.25$, (e) $x = 0.50$, and (f) $x = 0.75$ with s -like and p -like atomic orbital projections. (g) Primitive bulk 3D Brillouin zone with bulk high-symmetry points and (112) surface projected 2D Brillouin zone with corresponding surface high-symmetry points. Surface dispersion of $\text{Y}_{(1-x)}\text{Er}_x\text{PdBi}$ at strained thin-film lattice parameters for (h) $x = 0.25$, (i) $x = 0.50$, and (j) $x = 0.75$ with spectral weights denoting the surface contribution of electronic bands.

$Y_{(1-x)}Er_xPdBi$ ($x = 0.0, 1.0, 0.25, 0.50,$ and $0.75,$ respectively) at the experimental bulk lattice parameters [9,14]. In all the cases, a clear inversion between Γ_8 (p -like) and Γ_6 (s -like) bands is observed at the Γ -point. Hence, all the systems are expected to be topologically nontrivial with robust surface states. Pure YPdBi is diamagnetic and its bulk band structure is shown in Fig. 6(b). Due to absence of Er, there are no flat bands near the Fermi level (E_F) originating from Er $4f$ orbitals. In the case of pure ErPdBi, neutron-diffraction studies suggest type-II antiferromagnetic (AFM2) ordering with the magnetic moments aligned along the [111] direction or lying on the (111) plane of the cubic conventional cell [2,63]. Hence, we have considered AFM2 ordering for ErPdBi with moments aligned along the equivalent [111] direction of our simulation unit cell [2]. Bulk band structure of pure ErPdBi in AFM2 configuration is shown in Fig. 6(c). A few other magnetic orderings for pure ErPdBi (as shown in Fig. S11 [41]) were also simulated and AFM2 turned out to be most stable in accordance with the neutron-diffraction studies. Although a perfect magnetic ordering is not well defined for alloy systems, different substitutional configurations with compensated magnetic moments were considered for $Y_{(1-x)}Er_xPdBi$ ($x = 0.25, 0.50,$ and 0.75) with AFM2 as the base magnetic ordering. Interestingly, the lowest energy configurations are the ones where the majority species (Y/Er) cluster together (see Fig. S10 of the Supplemental Material [41] and related discussions therein). The electronic band structures of these configurations have been shown in Figs. 6(d)–6(f). Due to the presence of Er, flat bands originating from unfilled Er $4f$ orbitals begin to appear near E_F . Overall, it is seen that Er substitution in YPdBi enhances the strength of inversion between Γ_8 and Γ_6 bands, possibly due to s - f exchange interaction [64], which becomes maximum in pure ErPdBi. The $4f$ orbitals of Er appear as flat bands localized above E_F , and as the doping concentration (x) increases, more f bands start to appear near E_F that may also contribute to the increase in the band-inversion strength.

To simulate the thin-film nature of our samples, we have further calculated the dispersion of $Y_{(1-x)}Er_xPdBi$ ($x = 0.25, 0.50,$ and $0.75,$ henceforth referred to, respectively, as E25, E50, and E75 alloys) using the strained thin-film lattice parameters for the (112) surface of our simulation unit cell. The (112) surface of the simulation cell is equivalent to the (110) surface of the cubic conventional cell. The corresponding surface BZ is shown in Fig. 6(g). In pristine YPdBi and ErPdBi, all three atomic species (Y-Pd-Bi and Er-Pd-Bi, respectively) are terminated at the conventional (110) surface. In the case of alloys, there are three termination possibilities: Y-Pd-Bi, Er-Pd-Bi, and mixed Y-Er-Pd-Bi terminations. For the final chosen configurations of E25, E50 and E75 alloys, (110) surface can have either (i) Y-Er-Pd-Bi or Y-Pd-Bi termination, (ii) Er-Pd-Bi or Y-Pd-Bi termination, and (iii) Y-Er-Pd-Bi or Er-Pd-Bi termination, respectively. The simulated surface dispersions for Y-Er-Pd-Bi (E25 alloy), Er-Pd-Bi (E50 alloy), and Y-Er-Pd-Bi (E75 alloy) terminations are shown in Figs. 6(h)–6(j), respectively. Topologically nontrivial surface states (TSS) are clearly visible in all the dispersions and they increase with the increase in Er concentration. Several flat bands appear above E_F with high contribution from the surface and mix heavily with the

bulk electronic states. This bunch of flat bands moves away from E_F as the doping concentration increases. In the bulk, there is a crossing-like feature near E_F along the $L - \Gamma$ direction (see Fig. S12 [41]) that is projected onto the surface along the $\bar{Y} - \bar{\Gamma}$ direction. Nontrivial linear surface bands also appear around this crossing-like feature. Additionally, it is observed that there are TSS with less dispersion straddling E_F which originate from this crossing-like feature, especially in the E50 and E75 alloys. Flat bands are more likely to enhance superconductivity as higher effective mass of electrons could aid the formation of Cooper pairs. Existence of such dispersionless bands, both in the bulk and at the surface, strengthen the possibility of unconventional superconductivity. The E25 alloy has less TSS near E_F but the bunch of flat bands from Er $4f$ is relatively close to E_F [see Fig. 6(h)]. The situation is exactly opposite for the E75 alloy [see Fig. 6(j)] But, the E50 alloy seems to have optimal electronic dispersion at the surface near E_F [see Fig. 6(i)]. Additionally, the crossing-like feature in the bulk along the $L - \Gamma$ direction and projected along the $\bar{Y} - \bar{\Gamma}$ direction on the surface [see Fig. 6(i)] is very close to E_F compared to E25 and E75 alloys (see Fig. S12 [41]), which may lead to high mobility. It is well known that the SdH oscillations are a result of the oscillation of the density of states at(near) the Fermi level [54,65]. The nontrivial linear bands (along the $\bar{Y} - \bar{\Gamma}$ direction) are very close to the Fermi level for the E50 alloy as compared to E25 and E75 alloys. The presence of dispersionless bands near the nontrivial linear bands would further contribute to the density of states at the Fermi level, leading to a higher SdH oscillation amplitude in E50, as also observed in our experiments. Such optimal positioning of bands near E_F , both in bulk and at surface, could enhance superconducting properties for the E50 alloy as compared to E25 and E75 alloys. And our experiments indeed reveal the same.

V. CONCLUSION

We have presented the effect of f -electron doping on magnetotransport and electrical resistivity of YPdBi thin films. We observed variations in the superconducting and topological properties of Er-doped $Y_{(1-x)}Er_xPdBi$ ($x = 0.2, 0.5,$ and 0.8) films. The films show the variation of T_c with the concentration of Er, and a maximum of 4.4 K for E5 film. The T_c increases with a smaller concentration of Er, and then decreases at a higher concentration of Er; doping of $4f$ magnetic Er^{+3} ions on Y^{+3} sites increases electron density (n_{2D} of Table I), which may lead to an increase in T_c for E5 film [66]. At higher concentrations of Er, T_c decreases due to s - f exchange interaction. Since the odd-parity Cooper pair holds in YEPB films, hence s - f exchange interaction is taken into account [64]. As shown by Vonsovskii and Svirskii [64], the Hamiltonian for s - f exchange is correlated to the change in J ; it is expected that will impact the superconductivity and indirect exchange interaction in these Er-doped $Y_{(1-x)}Er_xPdBi$. DFT calculations show that the hybridization with localized $4f$ impurity levels induces effective repulsion between conduction electrons. The repulsion grows with the increasing impurity concentration, reducing the attractive pairing interaction between Cooper pairs, and leading to a decrease in T_c [67]. The increase of disorder at rare-earth sublattices is witnessed from

the decrease in coherence length (l), and transport lifetime (τ) (see Table I), which could validate the weakening of Cooper pairs at higher Er concentrations. The magnetotransport studies indicate the topological nontrivial nature of all E2, E5, and E8 semimetallic thin films, as also confirmed by our DFT calculations.

ACKNOWLEDGMENTS

S.S. acknowledges MHRD for financial support and NRF, CRF, PPMS, and PLD (Department of Physics) facilities at

IIT Delhi. B.D. acknowledges MHRD India and IIT Bombay for financial support. R.C. acknowledges the funding received from DST Nanomission Project. No. DST/NM/TUE/QM-11/2019 (RP03993G), and Indo-Swedish Joint Research Programme Grant No. DST/INT/SWD/VR/P-01/2019(RP04014) in support of research in this area. R.C. also acknowledges the financial assistance received from the Grant No. K2-2022-022 from NUST “MISIS,” Russia. B.D. thanks Dr. C. K. Barman for stimulating discussions and valuable suggestions.

-
- [1] S. Chadov, X. Qi, J. Kübler, G. H. Fecher, C. Felser, and S. C. Zhang, Tunable multifunctional topological insulators in ternary Heusler compounds, *Nat. Mater.* **9**, 541 (2010).
- [2] Y. Nakajima, Topological RPtBi half-Heusler semimetals: A new family of noncentrosymmetric magnetic superconductors, *Sci. Adv.* **1**, e1500242 (2015).
- [3] Y. Liu *et al.*, Zeeman splitting and dynamical mass generation in Dirac semimetal ZrTe₅, *Nat. Commun.* **7**, 12516 (2016).
- [4] C. Shekhar *et al.*, Anomalous Hall effect in Weyl semimetal half-Heusler compounds RPtBi ($R = \text{Gd}$ and Nd), *Proc. Natl. Acad. Sci. USA* **115**, 9140 (2018).
- [5] N. P. Butch, P. Syers, K. Kirshenbaum, A. P. Hope, and J. Paglione, Superconductivity in the topological semimetal YPtBi, *Phys. Rev. B* **84**, 220504 (2011).
- [6] Y. Tokura, K. Yasuda, and A. Tsukazaki, Magnetic topological insulators, *Nat. Rev. Phys.* **1**, 126 (2019).
- [7] T. Shirokura, T. Fan, N. H. D. Khang, T. Kondo, and P. N. Hai, Efficient spin current source using a half-Heusler alloy topological semimetal with back end of line compatibility, *Sci. Rep.* **12**, 2426 (2022).
- [8] S. M. A. Radmanesh, C. Martin, Y. Zhu, X. Yin, H. Xiao, Z. Q. Mao, and L. Spinu, Evidence for unconventional superconductivity in half-Heusler YPdBi and TbPdBi compounds revealed by London penetration depth measurements, *Phys. Rev. B* **98**, 241111 (2018).
- [9] V. Bhardwaj, A. Bhattacharya, S. Srivastava, V. V. Khovaylo, J. Sannigrahi, N. Banerjee, B. K. Mani, and R. Chatterjee, Strain driven emergence of topological non-triviality in YPdBi thin films, *Sci. Rep.* **11**, 7535 (2021).
- [10] G. Xu, W. Wang, X. Zhang, Y. Du, E. Liu, S. Wang, G. Wu, Z. Liu, and X. X. Zhang, Weak antilocalization effect and non-centrosymmetric superconductivity in a topologically nontrivial semimetal LuPdBi, *Sci. Rep.* **4**, 5709 (2014).
- [11] O. Pavlosiuk, D. Kaczorowski, and P. Wiśniewski, Shubnikov-de Haas oscillations, weak antilocalization effect and large linear magnetoresistance in the putative topological superconductor LuPdBi, *Sci. Rep.* **5**, 9158 (2015).
- [12] H. Xiao, T. Hu, W. Liu, Y. L. Zhu, P. G. Li, G. Mu, J. Su, K. Li, and Z. Q. Mao, Superconductivity in the half-Heusler compound TbPdBi, *Phys. Rev. B* **97**, 224511 (2018).
- [13] Y. Pan, A. M. Nikitin, T. V. Bay, Y. K. Huang, C. Paulsen, B. H. Yan, and A. de Visser, Superconductivity and magnetic order in the noncentrosymmetric half-Heusler compound ErPdBi, *EPL* **104**, 27001 (2013).
- [14] V. Bhardwaj, A. Bhattacharya, A. K. Nigam, S. P. Dash, and R. Chatterjee, Observation of surface dominated topological transport in strained semimetallic ErPdBi thin films, *Appl. Phys. Lett.* **117**, 132406 (2020).
- [15] A. Bhattacharya, V. Bhardwaj, B. K. Mani, J. K. Dutt, and R. Chatterjee, Strain-tunable triple point fermions in diamagnetic rare-earth half-Heusler alloys, *Sci. Rep.* **11**, 12029 (2021).
- [16] V. Bhardwaj, K.-M. Chen, Y.-C. Tseng, and R. Chatterjee, Study of Al interdiffusion in ultrathin β -Ta/Co₂FeAl/MgO heterostructures for enhanced spin-orbit torque, *Phys. B: Condens. Matter* **574**, 411662 (2019).
- [17] P. Hohenberg and W. Kohn, Inhomogeneous electron gas, *Phys. Rev.* **136**, B864 (1964).
- [18] W. Kohn and L. J. Sham, Self-consistent equations including exchange and correlation effects, *Phys. Rev.* **140**, A1133 (1965).
- [19] G. Kresse and J. Hafner, *Ab initio* molecular dynamics for liquid metals, *Phys. Rev. B* **47**, 558 (1993).
- [20] G. Kresse and J. Furthmüller, Efficient iterative schemes for *ab initio* total-energy calculations using a plane-wave basis set, *Phys. Rev. B* **54**, 11169 (1996).
- [21] G. Kresse and J. Furthmüller, Efficiency of *ab-initio* total energy calculations for metals and semiconductors using a plane-wave basis set, *Comput. Mater. Sci.* **6**, 15 (1996).
- [22] P. E. Blöchl, Projector augmented-wave method, *Phys. Rev. B* **50**, 17953 (1994).
- [23] G. Kresse and D. Joubert, From ultrasoft pseudopotentials to the projector augmented-wave method, *Phys. Rev. B* **59**, 1758 (1999).
- [24] J. P. Perdew, K. Burke, and M. Ernzerhof, Generalized gradient approximation made simple, *Phys. Rev. Lett.* **77**, 3865 (1996).
- [25] S. L. Dudarev, G. A. Botton, S. Y. Savrasov, C. J. Humphreys, and A. P. Sutton, Electron-energy-loss spectra and the structural stability of nickel oxide: An LSDA+U study, *Phys. Rev. B* **57**, 1505 (1998).
- [26] S. M. Saini, N. Singh, T. Nautiyal, and S. Auluck, Optical properties of heavy rare earth metals (Gd–Lu), *Solid State Commun.* **140**, 125 (2006).
- [27] S. Krishnaveni, M. Sundareswari, P. C. Deshmukh, S. R. Valluri, and K. Roberts, Band structure and transport studies of half Heusler compound DyPdBi: An efficient thermoelectric material, *J. Mater. Res.* **31**, 1306 (2016).
- [28] J. T. Pegg, A. E. Shields, M. T. Storr, A. S. Wills, D. O. Scanlon, and N. H. de Leeuw, Hidden magnetic order in plutonium dioxide nuclear fuel, *Phys. Chem. Chem. Phys.* **20**, 20943 (2018).
- [29] N. Marzari and D. Vanderbilt, Maximally localized generalized Wannier functions for composite energy bands, *Phys. Rev. B* **56**, 12847 (1997).

- [30] I. Souza, N. Marzari, and D. Vanderbilt, Maximally localized Wannier functions for entangled energy bands, *Phys. Rev. B* **65**, 035109 (2001).
- [31] N. Marzari, A. A. Mostofi, J. R. Yates, I. Souza, and D. Vanderbilt, Maximally localized Wannier functions: Theory and applications, *Rev. Mod. Phys.* **84**, 1419 (2012).
- [32] A. A. Mostofi, J. R. Yates, Y.-S. Lee, I. Souza, D. Vanderbilt, and N. Marzari, WANNIER90: A tool for obtaining maximally-localised Wannier functions, *Comput. Phys. Commun.* **178**, 685 (2008).
- [33] A. A. Mostofi, J. R. Yates, G. Pizzi, Y.-S. Lee, I. Souza, D. Vanderbilt, and N. Marzari, An updated version of WANNIER90: A tool for obtaining maximally-localised Wannier functions, *Comput. Phys. Commun.* **185**, 2309 (2014).
- [34] G. Pizzi *et al.*, WANNIER90 as a community code: New features and applications, *J. Phys.: Condens. Matter* **32**, 165902 (2020).
- [35] D. H. Lee and J. D. Joannopoulos, Simple scheme for surface-band calculations. I, *Phys. Rev. B* **23**, 4988 (1981).
- [36] D. H. Lee and J. D. Joannopoulos, Simple scheme for surface-band calculations. II. The Green's function, *Phys. Rev. B* **23**, 4997 (1981).
- [37] M. P. L. Sancho, J. M. L. Sancho, J. M. L. Sancho, and J. Rubio, Highly convergent schemes for the calculation of bulk and surface Green functions, *J. Phys. F: Met. Phys.* **15**, 851 (1985).
- [38] Q. Wu, S. Zhang, H.-F. Song, M. Troyer, and A. A. Soluyanov, WANNIERTOOLS: An open-source software package for novel topological materials, *Comput. Phys. Commun.* **224**, 405 (2018).
- [39] R. D. Shannon, Revised effective ionic radii and systematic studies of interatomic distances in halides and chalcogenides, *Acta Crystallogr., Sect. A* **32**, 751 (1976).
- [40] B. Joshi, A. Thamizhavel, and S. Ramakrishnan, Superconductivity in noncentrosymmetric BiPd, *Phys. Rev. B* **84**, 064518 (2011).
- [41] See Supplemental Material at <http://link.aps.org/supplemental/10.1103/PhysRevMaterials.8.075001> for auxiliary details on experimental synthesis, ac susceptibility, substrate superconductivity, demagnetization effects, longitudinal magnetoresistance, WAL effect, Dingle temperature, Landau-level fan diagram, simulation unit cells, simulated magnetic configurations, and electronic band structure at strained thin-film lattice parameters. References [68–70] have been cited in the Supplemental Material.
- [42] Y. S. Hor, A. J. Williams, J. G. Checkelsky, P. Roushan, J. Seo, Q. Xu, H. W. Zandbergen, A. Yazdani, N. P. Ong, and R. J. Cava, Superconductivity in $\text{Cu}_x\text{Bi}_2\text{Se}_3$ and its implications for pairing in the undoped topological insulator, *Phys. Rev. Lett.* **104**, 057001 (2010).
- [43] G. Zechner, K. L. Mletschnig, W. Lang, M. Dosmailov, M. A. Bodea, and J. D. Pedarnig, Unconventional critical state in $\text{YBa}_2\text{Cu}_3\text{O}_{7-\delta}$ thin films with a vortex-pin lattice fabricated by masked He^+ Ion beam irradiation, *Supercond. Sci. Technol.* **31**, 044002 (2018).
- [44] T. Klimczuk *et al.*, Superconductivity in the Heusler family of intermetallics, *Phys. Rev. B* **85**, 174505 (2012).
- [45] T. V. Bay, T. Naka, Y. K. Huang, and A. de Visser, Superconductivity in noncentrosymmetric YPtBi under pressure, *Phys. Rev. B* **86**, 064515 (2012).
- [46] F. F. Tafti, T. Fujii, A. Juneau-Fecteau, S. René de Cotret, N. Doiron-Leyraud, A. Asamitsu, and L. Taillefer, Superconductivity in the noncentrosymmetric half-Heusler compound LuPtBi: A candidate for topological superconductivity, *Phys. Rev. B* **87**, 184504 (2013).
- [47] T. V. Bay, T. Naka, Y. K. Huang, H. Luigjes, M. S. Golden, and A. de Visser, Superconductivity in the doped topological insulator $\text{Cu}_x\text{Bi}_2\text{Se}_3$ under high pressure, *Phys. Rev. Lett.* **108**, 057001 (2012).
- [48] V. Bhardwaj, N. Banerjee, and R. Chatterjee, Structural and transport properties of $\text{Y}_{1-x}(\text{Dy})_x\text{PdBi}$ ($0 \leq x \leq 1$) topological semi-metallic thin films, *Appl. Phys. Lett.* **119**, 122402 (2021).
- [49] V. Bhardwaj and R. Chatterjee, Topological materials, *Resonance* **25**, 431 (2020).
- [50] D. Mallick, S. Mandal, R. Ganesan, and P. S. Anil Kumar, Fermi level tuning and the robustness of topological surface states against impurity doping in Sn Doped $\text{Sb}_2\text{Te}_2\text{Se}$, *Appl. Phys. Lett.* **118**, 154001 (2021).
- [51] S. Hikami, A. I. Larkin, and Y. Nagaoka, Spin-orbit interaction and magnetoresistance in the two dimensional random system, *Prog. Theor. Phys.* **63**, 707 (1980).
- [52] V. Bhardwaj, S. P. Pal, L. K. Varga, M. Tomar, V. Gupta, and R. Chatterjee, Weak antilocalization and quantum oscillations of surface states in topologically nontrivial DyPdBi(110) half heusler alloy, *Sci. Rep.* **8**, 9931 (2018).
- [53] I. M. Lifshitz and A. M. Kosevich, Theory of magnetic susceptibility in metals at low temperature, *Sov. Phys. JETP* **2**, 636 (1956).
- [54] D. Shoenberg, *Magnetic Oscillations in Metals* (Cambridge University Press, New York, USA, 1984).
- [55] L. Onsager, Interpretation of the de Haas-van Alphen effect, *London Edinburgh Dublin. Philos. Mag. J. Sci.* **43**, 1006 (1952).
- [56] O. Pavlosiuk, D. Kaczorowski, X. Fabreges, A. Gukasov, and P. Wiśniewski, Antiferromagnetism and superconductivity in the half-Heusler semimetal HoPdBi, *Sci. Rep.* **6**, 18797 (2016).
- [57] N. V. Dai, N. C. Thuan, L. V. Hong, N. X. Phuc, Y. P. Lee, S. A. Wolf, and D. N. H. Nam, Impact of in-plane currents on magnetoresistance properties of an exchange-biased spin valve with an insulating antiferromagnetic layer, *Phys. Rev. B* **77**, 132406 (2008).
- [58] B. G. Park *et al.*, A spin-valve-like magnetoresistance of an antiferromagnet-based tunnel junction, *Nat. Mater.* **10**, 347 (2011).
- [59] S. M. Wu, S. A. Cybart, D. Yi, J. M. Parker, R. Ramesh, and R. C. Dynes, Full electric control of exchange bias, *Phys. Rev. Lett.* **110**, 067202 (2013).
- [60] T. Kampfrath, A. Sell, G. Klatt, A. Pashkin, S. Mährlein, T. Dekorsy, M. Wolf, M. Fiebig, A. Leitenstorfer, and R. Huber, Coherent terahertz control of antiferromagnetic spin waves, *Nat. Photon.* **5**, 31 (2011).
- [61] H. Qiu *et al.*, Terahertz spin current dynamics in antiferromagnetic hematite, *Adv. Sci.* **10**, 2300512 (2023).
- [62] E. Rongione *et al.*, Emission of coherent THz magnons in an antiferromagnetic insulator triggered by ultrafast spin-phonon interactions, *Nat. Commun.* **14**, 1818 (2023).
- [63] O. Pavlosiuk, X. Fabreges, A. Gukasov, M. Meven, D. Kaczorowski, and P. Wiśniewski, Magnetic structures of

- RE*PdBi half-Heusler bismuthides ($RE = \text{Gd, Tb, Dy, Ho, Er}$), *Phys. B: Condens. Matter* **536**, 56 (2018).
- [64] S. V. Vonsovskii and M. S. Svirskii, Theory of s-f exchange for nonvanishing orbital angular momenta, *Sov. Phys. JETP* **22**, 473 (1966).
- [65] J. M. Ziman, *Principles of the Theory of Solids* (Cambridge University Press, Cambridge, UK, 1972).
- [66] M. Meinert, Unconventional superconductivity in YPtBi and related topological semimetals, *Phys. Rev. Lett.* **116**, 137001 (2016).
- [67] N. E. Bickers and G. E. Zwicknagl, Depression of the superconducting transition temperature by magnetic impurities: Effect of Kondo resonance in the f density of states, *Phys. Rev. B* **36**, 6746 (1987).
- [68] T. Klimczuk, T. M. McQueen, A. J. Williams, Q. Huang, F. Ronning, E. D. Bauer, J. D. Thompson, M. A. Green, and R. J. Cava, Superconductivity at 2.2 K in the layered oxypnictide $\text{La}_3\text{P}_4\text{Ni}_4\text{O}_2$, *Phys. Rev. B* **79**, 012505 (2009).
- [69] R. A. Hein, T. L. Francavilla, and D. H. Liebenberg, *Magnetic Susceptibility of Superconductors and Other Spin Systems* (Springer, Boston, MA, USA, 1991).
- [70] M. M. Doria, E. H. Brandt, and F. M. Peeters, Magnetization of a superconducting film in a perpendicular magnetic field, *Phys. Rev. B* **78**, 054407 (2008).